














The Passage of the Solar System through the Edge of the Local Bubble

Merav Opher^{1,2} , Abraham Loeb³ , Catherine Zucker³ , Alyssa Goodman³ , Ralf Konietzka³ , Alexandra Z. Worden^{1,4} ,
Evan P. Economo^{1,5} , Jesse A. Miller² , João Alves⁶, Jonathan Grone⁷, Marc Kornbleuth² , J. E. G. Peek⁸ , and
Michael M. Foley³ 

¹ Radcliffe Institute for Advanced Studies at Harvard University, Cambridge, MA, USA; mopher@bu.edu

² Astronomy Department, Boston University, Boston, MA 02215, USA

³ Center for Astrophysics | Harvard & Smithsonian, 60 Garden Street, Cambridge, MA 02138, USA

⁴ Marine Biological Laboratory, Woods Hole, MA 02543, USA

⁵ Biodiversity and Biocomplexity Unit, Okinawa Institute of Science and Technology Graduate University, Japan

⁶ University of Vienna, Department of Astrophysics, Vienna, Austria

⁷ GEOMAR Helmholtz Centre for Ocean Research Kiel, Düsternbrooker Weg 20, 24105 Kiel, Germany

⁸ Space Telescope Science Institute, 3700 San Martin Drive, Baltimore, MD 21218, USA

Received 2023 June 6; revised 2024 June 1; accepted 2024 June 14; published 2024 September 10

Abstract

The Sun moves through the interstellar medium (ISM) at a velocity of ~ 19 pc Myr⁻¹, making the conditions outside the solar system vary with time over millions of years. Today's solar system is protected from interstellar particles by the heliosphere, the bubble formed by the solar wind as the Sun moves through the ISM, which engulfs the planets. There is geological evidence from ⁶⁰Fe that Earth was in direct contact with the ISM 2–3 and 5–7 million years ago (MYA). Recent work argues that the Sun encountered a massive cold cloud 2 MYA as part of the Local Ribbon of Cold Clouds that shrunk the heliosphere and exposed Earth to the ISM. Here, we consider the effects of the passage of the Sun through the edge of the Local Bubble occurring at $6.8_{-0.4}^{+0.5}$ MYA assuming that the Sun encountered a cloud with a density of 900 cm⁻³. If we consider additional turbulent motion within the cloud due to shocks, the density encountered can be as low as 283 cm⁻³. Clouds of this density cover a small but nonzero ($\lesssim 4.6\%$) fraction of the surface of the Local Bubble, making an encounter plausible. Using a state-of-the-art magnetohydrodynamic model, we show that the heliosphere shrank to a scale smaller than Earth's orbit, thereby exposing Earth to cold dense ISM, consistent with ⁶⁰Fe evidence. The timing of the event matches perturbations observed in the paleoclimate record recovered from deep-sea sediments. The passage through the Local Bubble's surface and contraction of the heliosphere therefore may have impacted the climate and biosphere significantly, suggesting a new driver of major events in Earth's history.

Unified Astronomy Thesaurus concepts: Solar wind (1534); Heliopause (707); Astrospheres (107); Interstellar medium (847); Magnetohydrodynamics (1964); Interstellar medium wind (848); Stellar winds (1636)

1. Introduction

Remarkable steps forward in understanding the Local Bubble—the interstellar cavity in which our solar system currently resides (Zucker et al. 2022)—have provided a framework for examining the trajectory of our solar system, and its encounters with variable Galactic conditions.

Our recent understanding of the Local Bubble builds on the works of Fuchs et al. (2006), Schulreich (2015), Breitschwerdt et al. (2016), and Schulreich et al. (2017). Brought into existence by supernovae ~ 14 million years ago (MYA), and expanding ever since, the Local Bubble has a low-density volume of interstellar medium (ISM), harbors warm clouds (with densities of neutral hydrogen ~ 0.2 cm⁻³; Frisch et al. 2009) and rare regions of dense cold clouds (~ 1000 cm⁻³; Haud 2010), and is bounded by an outer shell where most nearby star formation occurs (Zucker et al. 2022). More specifically, detailed knowledge of the evolution and extent of the Local Bubble has not only enabled detailed constraints on the evolution of star-forming bubbles as a cosmic process, but also provides the opportunity to develop and test hypotheses on Galactic encounters that impact the heliosphere. The latter, a

protective cocoon arising from the deflection of the Sun's winds as it transits through the ISM, is broadly recognized for its importance in shielding the stellar system from low-energy Galactic cosmic rays (GCRs) and interstellar dust. Indeed, today's heliosphere has been shown to shield Earth from 70% of GCRs with energies up to 200 MeV (Stone et al. 2019).

Previous studies (Florinski & Zank 2006) explored the consequences for the shielding of GCRs stemming from different ISM conditions, ranging from fully ionized to neutral hydrogen densities of $n_{\text{H}} = 15$ cm⁻³. The boundaries of the heliosphere react to different conditions of the ISM. Currently, the heliosphere is embedded in a partially ionized ISM ($n_{\text{H}} = 0.18$ cm⁻³) and extends in the nose direction to 130 au (Stone et al. 2008) engulfing all of the solar system's planets. Subjected to a much denser ISM ($n_{\text{H}} = 15$ cm⁻³), previous work (Muller et al. 2006; Zank & Frisch 1999) shows that the heliosphere shrank to 23 au, just within Neptune's orbit.

If the heliosphere was exposed to cold dense clouds throughout the Sun's trajectory, it potentially reduced in dimension to within Earth's orbit, exposing our planet to dense hydrogen in the ISM. This shrinkage, in turn, would have caused changes to the chemistry and climate of the Earth's atmosphere (Begelman & Rees 1976; McKay & Thomas 1978; Yeghikyan & Fahr 2004). Additionally, shrinking of the heliosphere would increase the flux of GCRs, energetic particles streaming through the Galaxy, reaching Earth.



Original content from this work may be used under the terms of the [Creative Commons Attribution 4.0 licence](https://creativecommons.org/licenses/by/4.0/). Any further distribution of this work must maintain attribution to the author(s) and the title of the work, journal citation and DOI.

Increased radiation levels would very likely affect Earth's climate and the biosphere. Thus, advancements for modeling Galactic interactions that impact the heliosphere are likely important for understanding shifts in climate and consequences for life on Earth.

Until recently the primary focus with respect to astronomical impacts on Earth's climate and biota has centered around those arising from changes in the tilt (obliquity) and orientation (precession) of the Earth's axis, as well as shifts of Earth's elliptical orbit (eccentricity). These orbital forcing mechanisms drive seasonal changes and have demonstrated roles in oscillations between arid and wet climatic regimes over periods $> 10^4$ – 10^5 yr due to changes in solar insolation. Other phenomena are known to drive climatic changes as well, such as impact from asteroids or volcanic dust in the atmosphere posteruption, and feedback loops between these various drivers. The consequences of climate perturbations are dramatic and can drive alteration of the carbon cycle, CO_2 uptake by terrestrial and marine organisms, as well as speciation, all of which are recorded at least to some extent in deep-sea sediments (Zachos et al. 2001; Westerhold et al. 2020).

There are climate shifts that have occurred for which the triggers are still unclear. A major anomaly in our understanding of Earth's recent history is highlighted by changes in $\delta^{13}\text{C}$ isotope ratios in foraminifera in deep-sea sediments. These data indicate periods of marked temperature reductions and changes in biological productivity at both 2–3 MYA and ~ 6.5 – 7.65 MYA. The latter period is known as Late Miocene carbon isotope shift (LMCIS) and Late Miocene cooling, wherein the material incorporated by biota clearly reflected temperature and drastic primary productivity shifts (Zachos et al. 2001; Westerhold et al. 2020). Additionally, geological data from ^{60}Fe and ^{244}Pu isotopes indicate Earth was in direct contact with the ISM during these two periods (Knie et al. 1999, 2004; Fitoussi et al. 2008; Wallner et al. 2016, 2021; Fimiani et al. 2016; Binns et al. 2016; Ludwig et al. 2016; Koll et al. 2019) and the presence of these isotopes has been attributed to the arrival of supernova ejecta (Fields et al. 2008; Schulreich 2015; Breitschwerdt et al. 2016; Wallner et al. 2021; Miller & Fields 2022).

We propose that the ^{60}Fe signals at 2 and 7 MYA correspond to periods where the Sun encountered conditions that ultimately resulted in Earth being exposed directly to the ISM. Regarding the 2 MYA event, recent research indicates that the Sun encountered a massive cold cloud that is part of the Local Ribbon of Cold Clouds (LRCC) at that time (Opher et al. 2024). After accounting for the uncertainties of the distance to the LRCC and the motion of the Sun, it was predicted that the Sun encountered the LRCC's tail end, toward the Lynx constellation (LxCC). Moreover, using the density of the best studied member of the LRCC, the Local Leo Cloud (Meyer et al. 2012), the authors found that the heliosphere shrunk to 0.22 au, smaller than the Earth's orbit around the Sun. The Earth then would have been exposed to ISM with neutral hydrogen densities $> 3000 \text{ cm}^{-3}$ at about 2 MYA, consistent with the geological record and likely having consequences for resident biota.

Here, we test the hypothesis that the crossing of the Sun through the edge of the Local Bubble caused the heliosphere to shrink to sub-astronomical-unit scales at ~ 7 MYA. This reduction could have left Earth and all other planets in our solar

system (apart from Mercury and Venus) exposed to the cold dense ISM, and led to direct contact with cold clouds. This event would then underpin observations of cosmic material in the geological record and climatic shifts on Earth at the time of crossing.

Another scenario that has been put forth to explain ^{60}Fe anomalies in general is that ^{60}Fe could penetrate the heliosphere and deposit on Earth via condensation onto dust grains without requiring shrinkage of the heliosphere to < 1 au (Fields et al. 2008; Fry et al. 2020; Wallner et al. 2021; Miller & Fields 2022; Athanassiadou & Fields 2011). Modeling of all the supernovae that have gone off inside the Local Bubble and the ^{60}Fe transport from them (Breitschwerdt et al. 2016) is outside the central premise of the work. In any case these alternative scenarios needs some fine tuning since the responsible supernova could not have exploded closer than 8 pc, which is the so called “kill radius” that would initiate a mass extinction (Gehrels et al. 2003).

In particular a “complete” delivery mechanism (particularly important for distant explosions) for ^{60}Fe to Earth, e.g., via dust, is still unclear. Some works, such as Fry et al. (2020) and Athanassiadou & Fields (2011) explored part of the dust grain delivery but only characterized how supernovae eject dust grains. However, how the dust grains get further processed in the ISM and exactly which type of grains will exist in “cold clouds,” such as the one we explore in this paper, still need to be examined and are beyond the scope of this work. In addition, there is the trajectory of dust entering the heliosphere that is subjected to the solar and terrestrial magnetic field, which needs further exploration (Slavin et al. 2012; Sterken et al. 2013). Finally, the role of the heliospheric current sheet (that divides regions of opposite polarities of the solar magnetic field) and its behavior in the heliosheath (HS) is not understood (e.g., Opher et al. 2011) and is in fact an active area of research (Opher et al. 2023).

Second, the timing of a close-in supernova explosion contradicts the model of Local Bubble formation (Zucker et al. 2022), which uses new 3D spatial and dynamical constraints from the Gaia mission to track the surviving members of the stellar clusters hosting the supernovae that created the Local Bubble. Zucker et al. (2022) find that the formation of the Local Bubble was driven by a series of ~ 15 supernovae that started exploding circa 14 MYA, but that the Sun did not cross these progenitor stellar clusters in the recent past, inconsistent with the idea that a supernova exploded within ~ 10 pc of the Sun (see interactive Figure 2 in Zucker et al. 2022). A supernova explosion farther than 10 pc will require more assumptions, such as the delivery of dust and its entry into the heliosphere as discussed above.

The organization of this paper is as follows. We first discuss the model used to simulate the encounter of the heliosphere with the edge of the Local Bubble (Section 2), then the simulation and the shrinking of the heliosphere (Section 3), and finally some possible implications of the shrinking (Section 4).

2. Model

We use a 3D state-of-the-art magnetohydrodynamic (MHD) model (Opher et al. 2015, 2024) to simulate the crossing of the heliosphere with the edge of the Local Bubble 7 MYA. The numerical model includes charge exchange between neutrals and ions, as well the Sun's gravity, which plays an important role of focusing the gas flow. Neutral H is included as a

multifluid description that is appropriate for these high densities (Zank 1999; Opher et al. 2009). The cold thermal solar wind and hot pickup ions (PUIs) are treated as a single species. The neutral hydrogen component is captured with a four-fluid approximation (Zank 1999; Opher et al. 2009). For the simulation in this paper, we only used the ISM neutral H component that is orders of magnitude more abundant than the HS and supersonic solar wind components.

The model solves a set of Euler’s equations for the different populations of neutral atoms and the ideal MHD equations for the plasma. The conservative form of the equations are solved by an explicit second-order spatiotemporal scheme, utilizing an HLLE-type Riemann solver developed by Linde (1998), for both the plasma and neutral fluids. A total-variation-diminishing principle is employed to reduce oscillations at discontinuities. The model employs a monotized central limiter with a typical beta parameter set at 1.5 (Sokolov et al. 2006). The impact of charge exchange processes is approximated through source terms to the continuity, momentum, and energy equations of the ideal MHD system (for more details and equations see Michael et al. 2022). The plasma solution is advanced in time accurate fashion.

We neglect radiation pressure from the Ly α line of hydrogen atoms since these cold dense clouds are optically thick to Ly α photons (Yeghikyan & Fahr 2006) with an optical depth τ much larger than unity; at the column density of hydrogen atoms $N \sim [900 \text{ cm}^{-3}] * [\text{pc}] \sim 10^{21} \text{ cm}^{-2}$. The Ly α cross section at resonance is $\sigma \sim 7 \times 10^{-11} \text{ cm}^2$ (Loeb & Rybicki 1999) and so $\tau \sim N\sigma \sim 10^{11}$. Hence, radiation was inferred to play a smaller role than gravity (same as in Yeghikyan & Fahr 2004). This is different than in current ISM conditions where radiation pressure is comparable to solar gravity (Schwadron et al. 2013). Additionally, we neglect photoionization, since its contribution is an order of magnitude smaller than that of charge exchange at these distances.

Future work can explore the current scenario with more advanced codes where the solar wind ions are treated as separate components (Opher et al. 2020) or the neutral hydrogen atoms are treated kinetically (Michael et al. 2022). We do not expect though any major changes from the current results. The density of neutrals is so high that a fluid treatment is appropriate. The separation of thermal and suprathermals will further enhance our results bringing the heliosphere further in. This is because PUIs exchange charge (the mean free path for keV PUIs is $\sim 0.01 \text{ au}^{-1}$ for densities as high as 900 cm^{-3}) and leave the system, deflating the heliosphere.

The domain of the model is $1500 \text{ au} \times 1500 \text{ au} \times 1500 \text{ au}$ cube in a Sun-centered frame.

The outer boundary conditions are set such that the ISM enters into the domain from the $x = -1500 \text{ au}$ face with outflow conditions, ensuring zero gradient of the fluid variables at the other faces. The inner boundary is placed at 0.1 au (or $21.5 R_{\odot}$). The adopted parameters of the solar wind at the inner boundary are $v_{\text{SW}} = 417 \text{ km s}^{-1}$, $n_{\text{SW}} = 5.71 \times 10^2 \text{ cm}^{-3}$, and $T_{\text{SW}} = 2.59 \times 10^5 \text{ K}$ based on the Alfvén-driven solar wind solution (Evans et al. 2012). The magnetic field is given by the Parker spiral magnetic field (Parker 1958) with $B_{\text{SW}} = 1.72 \times 10^2 \text{ nT}$ at the equator. We use a monopole configuration for the solar magnetic field (as in Izmodenov & Alexashov 2015; Opher et al. 2015). This description, while capturing the topology of the field lines, does not capture the change of polarity with solar cycle or across the heliospheric

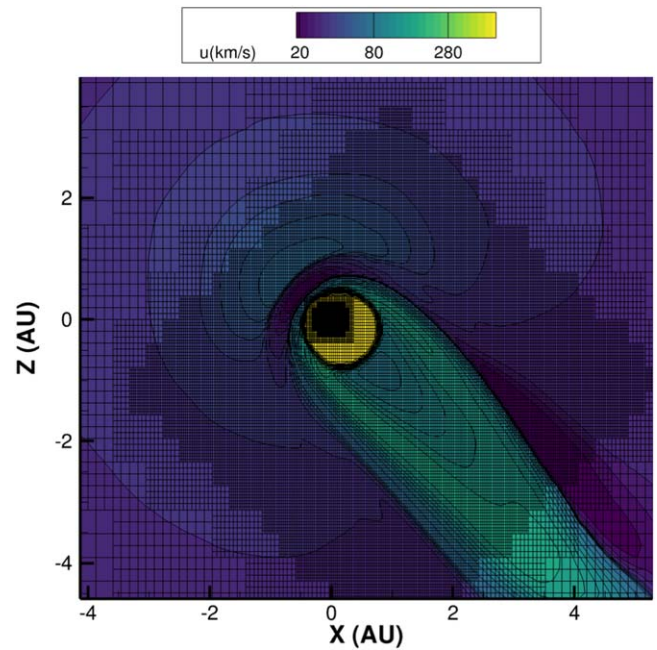


Figure 1. Grid is shown in a zoomed-in region around the region of interest in the meridional plane at $y = 0$.

current sheet. This choice, however, minimizes artificial reconnection effects, especially in the heliospheric current sheet. We assume that the magnetic axis is aligned with the solar rotation axis.

We use a nonuniform Cartesian grid that is adapted to ensure sufficient grid resolution. The grid is tilted (Figure 1) to align the highest resolution, which extends $\pm 50 \text{ au}$ in y and z and -20 – 50 au in x . We cover all regions of interest with high grid resolution (the minimum grid cell is in z near the inner boundary, 0.03 au in x , and 0.05 au in the region of interest, including the tail—see Figure 5). The numerical scheme is the second-order Linde scheme (Toth et al. 2012), so error bars are within two grid cells. The termination shock (TS) in the upstream direction is at $0.4 \pm 0.03 \text{ au}$. The resolution at the heliopause (HP) is 0.03 au so the location of the HP is at $0.7 \pm 0.06 \text{ au}$. The HS width is then $0.3 \pm 0.06 \text{ au}$ upstream—the tail direction was resolved with resolution of $\pm 0.03 \text{ au}$ extending to 3.2 au . In particular, the resolution used is more than sufficient to resolve the most important boundary; that is, the location of the HP upstream less than 1 au , i.e., $0.7 \pm 0.06 \text{ au}$. If the cloud would be partially molecular instead of atomic H—as we expect it to be given the presence of molecular gas in clouds on the bubble’s surface in the present day (see Section 4)—then one should consider the effect of charge exchange and temperature at these close distances. This is left for future work.

3. The Encounter of the Heliosphere with the Edge of the Local Bubble

To simulate the crossing, we used the model described in the previous section. For the simulation we need to estimate the relative motion of the Sun with respect to the Local Bubble to estimate the speed with which the neutral H atoms streamed into the heliosphere as a result of the encounter.

Because the Sun’s motion through the local standard of rest (LSR) in Galactic coordinates (U , V , W) is uncertain, in

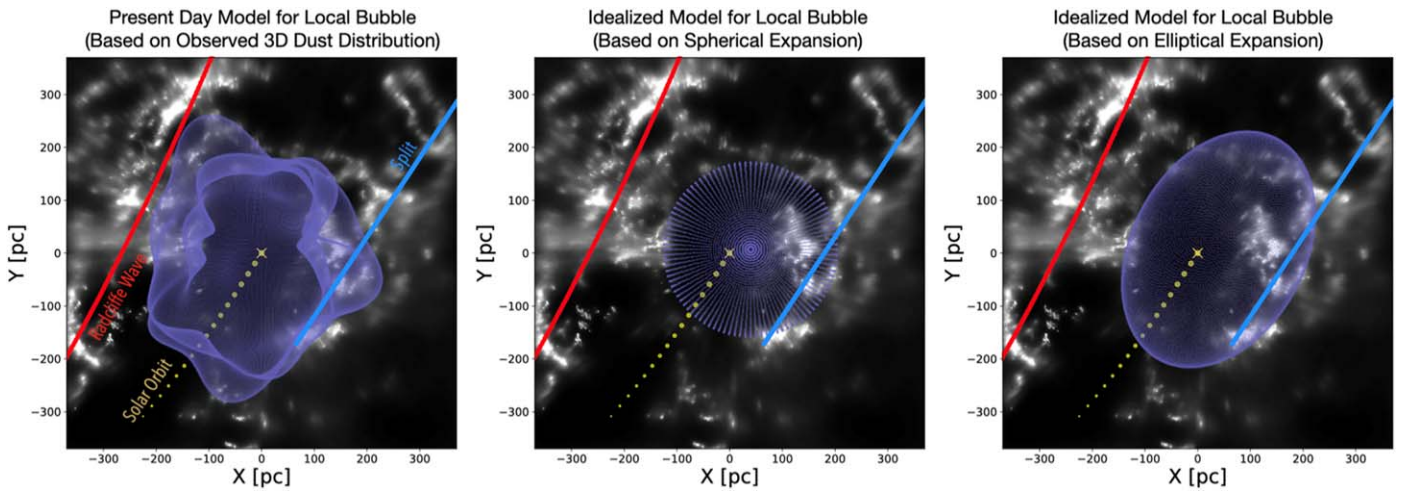


Figure 2. Left: a top-down view of the solar neighborhood, showing the 3D dust distribution (gray background; Leike et al. 2020) alongside models for the Radcliffe Wave (red curve; Alves et al. 2020) and the Split (blue curve; Lallement et al. 2019). In purple, we overlay a present-day model for the Local Bubble (Pelgrims et al. 2020) based on the observed 3D dust distribution (Lallement et al. 2019). We also overlay the solar orbit, which lies parallel to the Radcliffe Wave and the Split. In the middle and right panels, we show an idealized present-day model for the Local Bubble assuming either a spherical expansion (Zucker et al. 2022) or an elliptical expansion (this work). Since the bubble will expand faster toward lower-density regions (parallel to the Radcliffe Wave and the Split), the elliptical model may better capture the irregular expansion of the bubble in a nonuniform medium.

particular in the V component (Wang et al. 2020; Francis & Anderson 2009), we take the Sun’s motion as (10.0, 15.4, 7.8) km s^{-1} or a net speed of 19.9 pc Myr^{-1} for the motion of the Sun with respect to the LSR as in Zucker et al. (2022), which was taken from Kerr & Lynden-Bell (1986).

The Local Bubble has a very irregular surface with some locations potentially breaking out of the disk and forming a Galactic chimney (Pelgrims et al. 2020; Zucker et al. 2022). The Local Bubble is also expanding. To get the exact heliosphere crossing time, we need to consider its expansion speed as well as estimate its wall location in the direction of the Sun’s motion. The surface of the Local Bubble in the Galactic center and anticenter directions is currently expanding into two large-scale Galactic features, the Radcliffe Wave (Alves et al. 2020) and the Split (Lallement et al. 2019), which correspond to sections of a nearby spiral arm and spur, respectively (see Figure 1 of Zucker et al. 2023 for more details on the architecture of gas in the solar vicinity).

When calculating the expansion of the Local Bubble, previous studies (Zucker et al. 2022) assumed that the bubble is expanding spherically into a uniform ambient density medium, which is not the case given the existence of the Radcliffe Wave and the Split. In this work, we no longer assume a uniform ambient density, and instead assume the bubble is expanding elliptically, by modifying the solution from Zucker et al. (2022) based on the fact that the bubble will travel slower into regions of higher density (toward the Radcliffe Wave and the Split) and faster into regions of lower density (parallel to the Radcliffe Wave and the Split, along the Sun’s direction of motion) as shown in Figure 2.

To account for variable expansion of the Local Bubble due to these extant Galactic-scale features, we computed the density contrast between the Radcliffe Wave (Alves et al. 2020) and Split (Lallement et al. 2019) large-scale structures, and everything else in the present day. To compute the density contrast, we utilize the 3D dust map of Leike et al. (2020), which charts the 3D distribution of the local ISM at parsec-scale resolution.

We find that in the present day the Radcliffe Wave and Split are $\sim 6\times$ denser than the surrounding ISM within 400 pc. Based on the 3D positions, 3D space motions, and ages of young stellar clusters forming along the Radcliffe Wave and the Split in the Local Bubble’s expanding shell, previous work inferred an ambient density of 2.7 cm^{-3} at the time of the first supernova explosion circa 14 MYA (Zucker et al. 2022). If we assume a constant contrast in density as a function of time since the first supernova explosion, we would expect the density to be $6\times$ less, or $\sim 0.44 \text{ cm}^{-3}$ in the direction of the Sun, given that the Sun is currently traveling in a “valley” parallel to the Radcliffe Wave and Split large-scale structures.

To compute how fast the Local Bubble expands toward the direction of the Sun, we built on recent literature and use an analytic model (El-Badry 2019) for the radius, R , of the Local Bubble’s expanding shell as a function of time t , already applied in previous work (Zucker et al. 2022):

$$R(t) \approx 83 \text{ pc} (1 - \theta)^{1/5} \left(\frac{\text{ESN}}{10^{51} \text{ erg}} \right)^{1/5} \times \left(\frac{\Delta t \text{SNe}}{0.1 \text{ Myr}} \right)^{-1/5} \left(\frac{n_0}{1 \text{ cm}^{-3}} \right)^{-1/5} \left(\frac{t}{1 \text{ Myr}} \right)^{3/5}. \quad (1)$$

We adopt the free parameters of the model based on previous work (Zucker et al. 2022), leading to a cooling efficiency at the shell surface θ of 0.7, a time interval between supernova explosions $\Delta t \text{SNe}$ of 1.06 Myr, and an energy input per supernova explosion ESN of 10^{51} erg. We use an ambient medium density of 0.44 cm^{-3} given the $6\times$ lower ambient medium density in the direction of the Sun’s trajectory. In Figure 2, we show the 3D distribution of dust from Leike et al. (2020), the solar orbit, a present-day model for the Local Bubble (Pelgrims et al. 2020) based on 3D dust, the large-scale Radcliffe Wave (Alves et al. 2020) and Split (Lallement et al. 2019) features, and both the spherical (Zucker et al. 2022) and elliptical (this work) idealized models for the Local Bubble’s expansion. While our treatment of the bubble’s expansion is simple compared to hydrodynamic simulations (e.g., Schulreich et al. 2023), it is a plausible model that may better

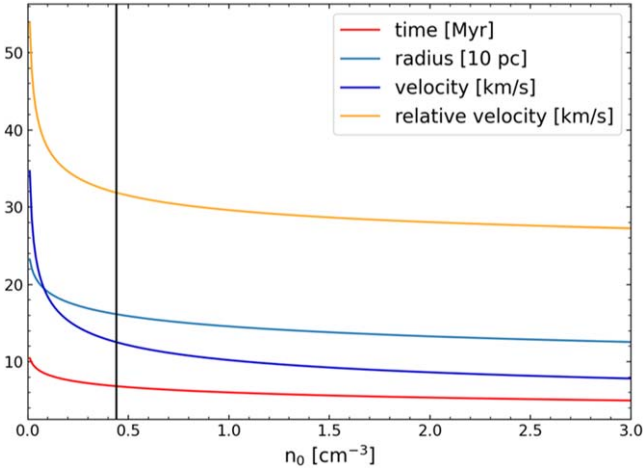


Figure 3. Plot shows the calculated change of the velocity and radius of the bubble, the crossing time, and the relative velocity observed from the Sun as a function of the ambient density n_0 . The black line indicates the ambient medium density along the Sun’s trajectory used in this work. The the y-axis labels are in the legend.

describe the irregular expansion of the bubble in a nonuniform medium based on the actual observed present-day density distribution in the solar neighborhood.

Accordingly, adopting the new elliptical model for expansion, the velocity of the shell at time t is then given as:

$$v(t) \approx 49.8 \text{ km s}^{-1} (1 - \theta)^{1/5} \left(\frac{\text{ESN}}{10^{51} \text{ erg}} \right)^{1/5} \times \left(\frac{\Delta t \text{ SNe}}{0.1 \text{ Myr}} \right)^{-1/5} \left(\frac{n_0}{1 \text{ cm}^{-3}} \right)^{-1/5} \left(\frac{t}{1 \text{ Myr}} \right)^{-2/5}. \quad (2)$$

We trace back the trajectory of the Sun using the `galpy` (Bovy 2015) package, which supports orbital integrations in a Milky Way–like potential consisting of a bulge, a disk, and a dark matter halo. We investigate the trajectory of the Sun from -10 MYA to the present day. By using the above mentioned ambient medium density together with Equations (1) and (2), we find the crossing time with the Local Bubble to be 6.8 Myr. It is important to note that `galpy` only considers the gravitational potential of the Galaxy as a whole but no local gravitational effects of the surrounding gas clouds. However, recent results of numerical simulations show that stellar orbits can be recovered with high accuracy up to 20 Myr in the past, even without explicitly modeling nonaxisymmetric components of the potential (Kamdar et al. 2021). Therefore, `galpy` is appropriate for tracing the trajectory of the Sun back in time 10 MYA.

The change of the Sun bubble-crossing time with ambient medium density n_0 is shown in Figure 3. We also show the change of the shell’s radius and velocity at the moment of the Sun bubble crossing with the ambient medium density n_0 , as well as the relative shell velocity observed from the Sun.

Computing how fast the Local Bubble would be expanding toward the Sun’s direction given this $6\times$ lower ambient density, we get a crossing time of 6.8 MYA and an expansion speed of $(U, V, W)_{\text{bubble}} = (-8.5, -8.8, -2.6) \text{ km s}^{-1}$. This provides the relative velocity between the Sun and the bubble of $(\Delta U, \Delta V, \Delta W) = (-18.5, -24.2, -10.4) \text{ km s}^{-1}$ or a magnitude of 32.2 km s^{-1} . Using the error bars on the ambient

density ($2.71_{-1.02}^{+1.57} \text{ cm}^{-3}$) from previous work the error bounds for the velocity would be $32.2_{-1.3}^{+1.7} \text{ km s}^{-1}$. For the crossing time the error bounds would be $6.8_{-0.4}^{+0.5} \text{ MYA}$.

Such relative velocities between the Sun and the Local Bubble correspond to Galactic coordinates of (longitude, latitude) = $(226^\circ.16, 50^\circ.11)$. Converting from Galactic to ecliptic coordinates⁹ for the J2000 epoch corresponds to latitude and longitude in ecliptic coordinates of (latitude, longitude) = $(1^\circ.46, 150^\circ.48)$. We finally need then to convert that to the heliocentric inertial (HCI) coordinate system (our model); this corresponds to (latitude, longitude) = $(-50^\circ.81, 12^\circ.02)$ or the coordinate vector $(x_{\text{HCI}}, y_{\text{HCI}}, z_{\text{HCI}}) = (0.62, 0.13, -0.78)$. This corresponds to the relative speeds in the HCI of $U_{x\text{-HCI}} = 19.89 \text{ km s}^{-1}$, $U_{y\text{-HCI}} = 4.24 \text{ km s}^{-1}$, and $U_{z\text{-HCI}} = -24.95 \text{ km s}^{-1}$. We then rotate the frame such that there is no flow in the y-component. We do this by taking the magnitude of the x and y velocity components and setting $U_{x\text{-HCI}}$ equal to this magnitude. Heliographic coordinate systems (Burlaga (1984) use the position of the solar rotation axis, which is defined by its decl. and R.A. with respect to the celestial pole. The HCI system is set such that the x–y plane lies in the solar equator in J2000.0, with the x-axis along the direction of the interstellar wind, the z-axis along the solar rotation axis, and the y-axis completing the right-handed coordinate system.

We assume that the Sun encountered a cloud with a density of 900 cm^{-3} as it crossed the edge of the Local Bubble. This density is the minimum value needed assuming that the cloud’s motion is equivalent to the bulk motion of the expanding wall of the Local Bubble. As discussed below, considering that the cloud could have an additional speed of 5 km s^{-1} beyond this bulk motion will allow for densities as low as 283 cm^{-3} to collapse the heliosphere. We do not attempt to model the entirety of the Local Bubble. Such simulations have been performed by e.g., Breitschwerdt et al. (2016), Schulreich et al. (2017), and Zucker et al. (2022). Instead, we model the passage of the solar system through a cloud on the edge of the Local Bubble. The edge of the Local Bubble will be a result of multiple supernova shocks. While no known clouds currently exist at this density in the direction of the Sun’s backward orbital trajectory, we presently see clouds with densities much greater than 900 cm^{-3} , harboring newly formed stars less than a few million years old, elsewhere on the surface of the bubble (largely cospatial with the Radcliffe Wave and the Split). Molecular cloud lifetimes can be as short as 5–7 Myr (Benincasa et al. 2020), so it is plausible that high-density (900 cm^{-3}) clouds that have since dispersed existed along the Sun’s path when it entered the Local Bubble, 7 MYA.

For the ISM outside the heliosphere, we then adopt $n_{\text{H}} = 900 \text{ cm}^{-3}$ and $T = 20 \text{ K}$. We include a negligible ionized component ($n_i = 0.01 \text{ cm}^{-3}$ and $T = 1 \text{ K}$) and ignore the presence of the interstellar magnetic field since its pressure is negligible compared to the ram pressure of the Local Bubble.

If the cloud would be partially molecular instead of atomic H, one should consider the effect of charge exchange and temperature at these close distances. This is left for a future work.

At large distances in the MHD simulations the ram pressure of neutral H is $P_{\text{ram}} = 5.2 \times 10^{-10} \text{ Pa cm}^{-2}$. (The thermal pressure of neutral H is $3.3 \times 10^{-15} \text{ Pa cm}^{-2}$.) At the HP the

⁹ http://lambda.gsfc.nasa.gov/toolbox/conv_coordinate.cgi

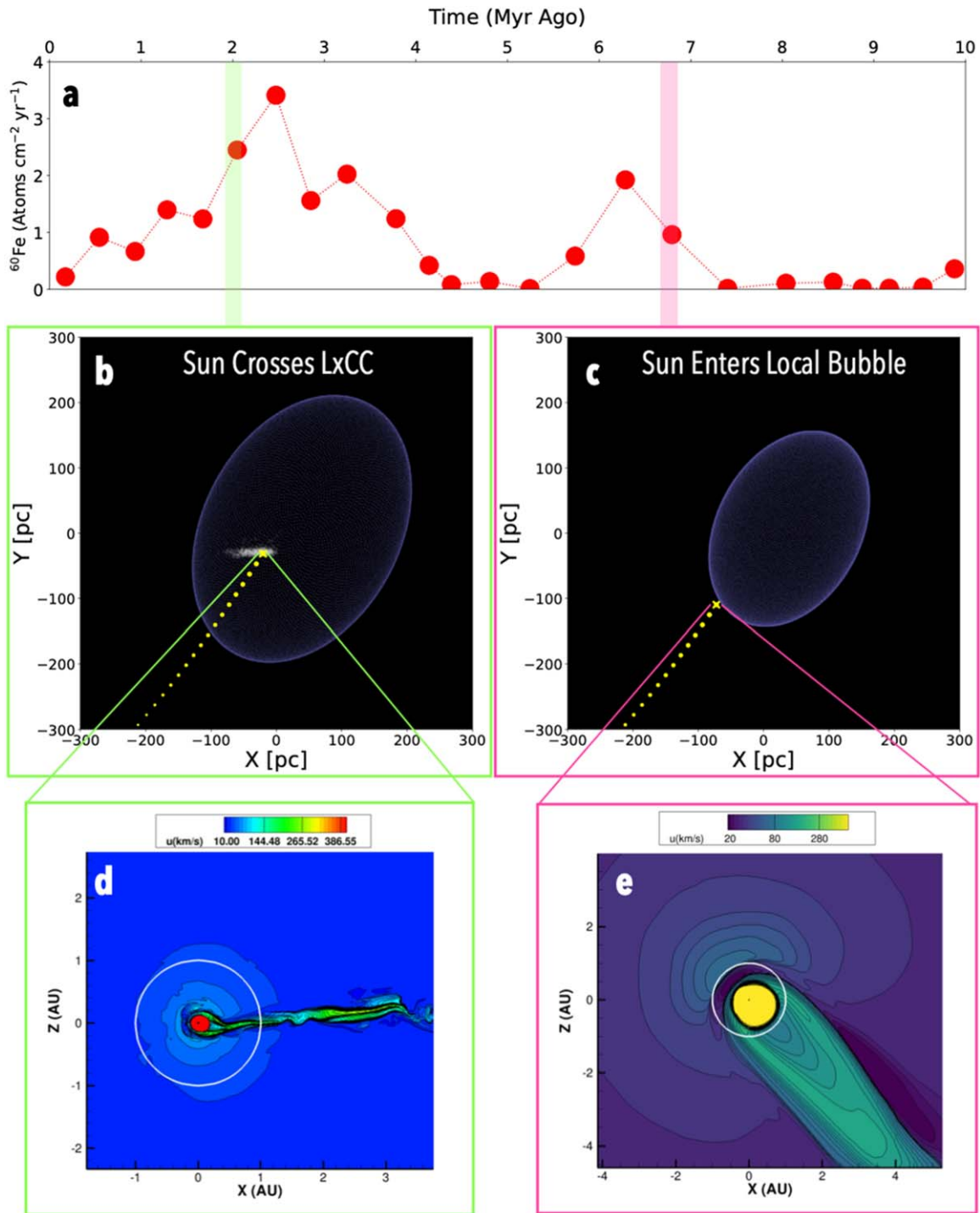


Figure 4. Evolution of the Sun and the dense ISM at two time snapshots occurring 2 MYA (panel (b)) and 7 MYA (panel (c)). We run two independent MHD simulations based on the backward trajectories of two different interstellar structures (the LxCC and the Local Bubble’s shell). The motion of the LxCC is exclusively discussed in Opher et al. (2024). The motion of the Local Bubble is constrained in this work, based on a modification to the original expansion described in Zucker et al. (2022). In both cases, the Sun’s trajectory is determined to cross the 3D trajectory of the clouds at locations/times that may coincide with peaks in ^{60}Fe . Under this premise, we run two independent MHD simulations given assumptions about the density of the LxCC and the Local Bubble’s shell and constraints on the relative velocities between the Sun and these interstellar structures. The purple surface in both panels shows an idealized model for the elliptical expansion of the Local Bubble. 7 MYA (panel (c)), the Sun entered the surface of the Local Bubble, shrinking the heliosphere to 0.7 au and exposing the Earth (white orbit) to the dense, cold ISM. Then, 2 MYA the Sun passes through the LxCC (panel (b)), shrinking the heliosphere to 0.22 au (panel (d)) and again exposing the Earth to the dense, cold ISM. The interactions between the Sun and the bubble’s surface/LxCC are consistent with the ^{60}Fe records (panel (a), adapted from Figure 1 of Wallner et al. 2021), which shows two peaks at ~ 2 –3 MYA and ~ 6 –7 MYA. An interaction version of panels (b) and (c) showing the full time progression of the Sun and the idealized bubble’s surface is available at https://faun.rc.fas.harvard.edu/czucker/Paper_Figures/Local_Bubble_Sun_Crossing_Opher23.html. The time sequence can be played forward or backward and has buttons to go to specific times. Links on the right can be clicked to turn various portions of the interactive figure on or off.

ram pressure of n_{H} is $P_{\text{ram}} = 1.55 \times 10^{-9} \text{ Pa cm}^{-2}$ and the thermal pressure is $1.24 \times 10^{-11} \text{ Pa cm}^{-2}$. For $10 \mu\text{G}$ the magnetic pressure, $P_{\text{mag}} = 6.9 \times 10^{-13} \text{ Pa cm}^{-2}$ orders of

magnitude smaller than the other pressures, so neglecting magnetic field is warranted as well. The run was performed for 2.7 yr.

In the encounter with the edge of the Local Bubble the heliosphere nose in the simulation shrank to 0.7 au (Figures 4 and 5(A)) exposing Earth and all the planets (besides Mercury and Venus) to dense cold ISM material for most of their trajectory. The supersonic solar wind goes through a TS (Figure 6) before reaching equilibrium with the cold ISM. The heliosphere tail is long and comet-like—the solar magnetic field at these distances is mostly radial and there is no confinement of the HS flow by the solar magnetic field. With these high neutral H densities, the mean free path is ~ 0.01 – 0.1 au (Figure 6(A)) and the neutrals get depleted quickly across the HP (Figure 6(B)), setting a strong gradient of ram pressure. The heliosphere reaches equilibrium with the cold ISM at the HP between the compressed solar magnetic field and the ram pressure of neutrals ahead of the HP. Gravity increases the density of neutrals from 900 cm^{-3} and a speed of 32.1 km s^{-1} at large distances to 995 cm^{-3} and a speed of 48.9 km s^{-1} near the HP (see Figures 6(A) and (B)).

Due to gravity the neutral density increases as the cold cloud encounters the heliosphere. One can estimate analytically the standoff distance (Baranov et al. 1979) as $\approx r_E \sqrt{\frac{\rho_E v_E^2}{\rho_\infty v_\infty^2}}$ where r_E , v_E , and ρ_E are the radius, speed, and density of the solar wind at Earth, respectively, and ρ_∞ and v_∞ are the density and speed at infinity of the ISM, respectively. Taking the values of $\rho_E = 5.71 \text{ cm}^{-3}$, $v_E = 417 \text{ km s}^{-1}$, $\rho_\infty = 900 \text{ cm}^{-3}$, and $v_\infty = 32.1 \text{ km s}^{-1}$ one gets that the standoff distance is 1.1 au. The neutral densities due to gravity increases to 995 cm^{-3} ahead of the heliosphere and the neutral speed to 48.9 km s^{-1} , bringing the same estimate of 0.65 au, which agrees very well with the simulation results.

If one adopts a relative speed between the Sun and the cloud to be as high as $\sim 37.2 \text{ km s}^{-1}$, and also assumes an increase of 52% in the relative speed and increase of density of 10% due to gravity as the neutrals approach Earth, then the density of the cloud needed to bring the standoff distance to sub-astronomical-unit scales is reduced to $\geq 283 \text{ cm}^{-3}$.

To arrive at a relative speed of $\sim 37.2 \text{ km s}^{-1}$ between the cloud and the Sun, we refer to 3D hydrodynamic simulations of isolated shocks passing into turbulence (Foley et al. 2024). The simulations were run by passing a shock of a given Mach number into turbulence of a given Mach number to analyze the velocity and density structure of the shock front using the moving-mesh code *Arepo* (Springel 2010). The adaptive nature of the *Arepo* mesh makes the code ideal for the study of dense regions in shocks. From this simulation suite, we choose snapshots that roughly match the structure of the Local Bubble moving into ambient turbulent gas at the time of the Sun’s crossing. As the simulations are scale-free, a sound speed and length scale can be adopted to match our physical model. Namely, our simulated shock is scaled to have a velocity of 12 km s^{-1} (expansion of the shell in the LSR frame at time of crossing) and a width of 23 pc (see Extended Data Figure 1 of Zucker et al. 2022), giving the ambient turbulent medium into which the shock propagates an average velocity of 5 km s^{-1} , a typical value for turbulence in the cold neutral medium. From this simulation, we find that gas in the shock front can travel as quickly as 17 km s^{-1} in the direction of shock propagation due to the combination of turbulent motion and coherent shock motion. Attributing an additional 5 km s^{-1} to the cloud’s motion due to the turbulence and coherent shocks, we estimate the Sun’s relative motion to the cloud could be as high as 37.2 km s^{-1} .

The heliosphere is so close to the Sun that the solar magnetic field is radial and HS plasma confinement does not take place (Opher et al. 2015). The flow in the HS is fast (~ 130 – 180 km s^{-1} , Figure 6) and the ram pressure is larger than the magnetic pressure. Because of the short mean free path, there are almost no neutrals inside the heliosphere and the density gradient in the HS is absent as well. The TS shifts to distances as close as 0.4 au from the Sun.

4. Probability of Such an Encounter

In order to determine whether this physical scenario is viable from a density standpoint, we estimate the cross section of the Sun encountering a cloud with a typical density of $\sim 283 \text{ cm}^{-3}$ as it passes through superbubbles like the Local Bubble. Specifically, we calculate the ratio of the surface area of molecular clouds on the surface of the Local Bubble over the bubble’s total surface area that falls within $|z| < 72$ pc of the disk. This is an estimate of the maximum displacement the Sun has reached in the last 10 Myr, calculated by following the methodology of Bahcall & Bahcall (1985) and incorporating updated properties of the Galactic potential near the Sun (see Konietzka et al. 2024).

We adopt the recent set of 3D volumetric models of solar neighborhood molecular clouds from Cahlon et al. (2024; based on the parsec-scale resolution 3D dust map from Leike et al. 2020) alongside the 3D model for the surface of the Local Bubble from Pelgrims et al. (2020). Specifically, we take all (x, y, z) points defining the surface of the Local Bubble (as defined by Pelgrims et al. 2020) that lie within $|z| < 72$ pc and project them onto an (l, b) map of the sky by generating a 2D histogram over the range ($l = -180^\circ, 180^\circ$) and ($b = -90^\circ, 90^\circ$) with a binning of 1 deg^2 . We then take every (x, y, z) point within every cloud in the Cahlon et al. (2024) catalog (see the 3D cloud segmentation table in Cahlon 2024¹⁰) that lies within a distance of 50 pc of the bubble’s surface ($\sim 2 \times$ the shell’s estimated 23 pc thickness) and within $|z| < 72$ pc, and likewise generate a 2D histogram using the same binning scheme. For both binning schemes, any (l, b) bin containing at least one bubble or cloud point is considered part of the bubble or cloud for the purpose of computing a surface area mask. We then take the ratio of the fraction of the sky included in the cloud mask over the fraction of the sky included in the bubble mask to compute ratio of 4.6%.

We consider the ratio of 4.6% to be an upper limit. The volumes occupied by the Cahlon et al. (2024) molecular clouds are defined above a density threshold of 25 cm^{-3} , well below the necessary density of 283 cm^{-3} required to shrink the heliosphere. However, we know the Cahlon et al. (2024) cloud volume densities (based on the 3D dust map of Leike et al. 2020) are underestimated because the 3D dust maps are known to “saturate” at densities of $\sim 50 \text{ cm}^{-3}$, due to limitations of 3D dust maps relying on optical stellar photometry and astrometry from Gaia (see Zucker et al. 2021). As a result, many of the Cahlon et al. (2024) clouds on the bubble’s surface must have volume densities greater than 283 cm^{-3} because they have previously been shown to be CO bright, and CO emission typically traces gas densities ~ 500 – 1000 cm^{-3} (see, e.g., Clark et al. 2019). The CO-bright clouds included in our calculation include, but are not limited to, the Chamaeleon, Coalsack, Lupus, Ophiuchus, and Taurus molecular cloud

¹⁰ <http://10.7910/DVN/BFYDG8>

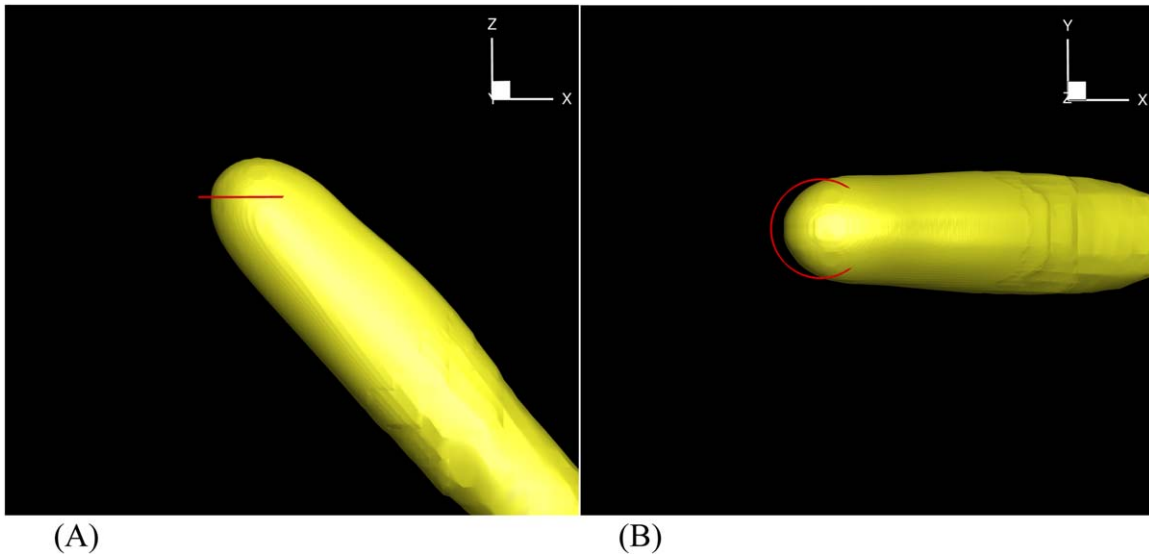


Figure 5. 3D image of heliosphere with two views: (A) side view and (B) top view. The trajectory of Earth is plotted in red. The isosurface of the heliosphere is plotted with a neutral hydrogen density of 736 cm^{-3} . We plotted the tail out to 3.2 au. The heliosphere nose is pushed in to 0.7 au.

complexes, all of which are CO bright according to Dame et al. (2001, see their Figure 2). Therefore, while we are unable to constrain the exact covering fraction given uncertainties in the 3D dust-based volume density estimates, we argue that an upper limit of $\lesssim 4.6\%$ is not unreasonable given the significant presence of CO-bright gas. The upper limit accounts for the fact that there is also the probability to encounter a shock moving 5 km s^{-1} faster than the average.

Therefore, computing this ratio of presumed molecular gas to the total bubble surface area in the present day, we find that $\lesssim 4.6\%$ of the surface area of the bubble within $|z| < 72 \text{ pc}$ is covered with molecular clouds potentially capable of shrinking the heliosphere. Assuming a similar ratio at the time of crossing, there is roughly a $\lesssim 4.6\%$ probability that the Sun would have encountered such a cloud 7 MYA. Future work combining the 3D density structure of these molecular clouds with their kinematics obtained from spectral-line gas maps (see, e.g., Tchernyshyov & Peek 2017) should enable improved modeling of the clouds' relative velocities to the Sun and further refinement of this picture.

5. Discussion and Possible Implications

We show that as a result of the encounter of the heliosphere with the edge of the Local Bubble the heliosphere shrinks to sub-astronomical-unit scales. The levels of ^{60}Fe expected to be deposited on Earth from encountering the edge of the Local Bubble (and associated reductions in heliosphere protection) at 7 MYA is consistent with the fluence of ^{60}Fe reported previously (Wallner et al. 2021). Moreover, this is consistent with the scenario of formation of the Local Bubble 14 MYA with 15 supernova explosions (see the Appendix). Additionally, the occurrence of the LMCIS between ~ 7.65 and 6.5 MYA is coincident with our findings pointing to reduced heliosphere protection in the same time period.

One important aspect to consider is the question of timescale and duration of the signal of ^{60}Fe versus the duration in which the Sun will remain inside a dense cloud. In Cahlon et al. (2024), the radius of each cloud is computed (see their Table 1), so by taking the mean cloud radius and the spread in cloud radii for all clouds that lie on the surface of the Local Bubble,

we can obtain an upper limit on the crossing time. We can only obtain an upper limit because we cannot directly constrain what fraction of the Cahlon et al. (2024) clouds are above a density of 283 cm^{-3} . We find a mean cloud radius of 6 pc, with a minimum and maximum cloud radius of 4 and 11 pc for the clouds used in the probability calculation of $\lesssim 4.6\%$ described above. Obtaining the diameters of the clouds from their radii, and adopting a velocity of 37 km s^{-1} , we get an upper limit on the range of crossing times, spanning 0.2–0.6 Myr, with a mean crossing time of 0.3 Myr.

This timescale is broadly consistent with the duration of the ^{60}Fe pulses ($\sim 1 \text{ Myr}$). This is consistent with prior studies of our passage through molecular clouds (e.g., McKay & Thomas 1978; Yeghikyan & Fahr 2004; Pavlov et al. 2005), which have estimated that crossing a giant molecular cloud takes of order 10^5 – 10^6 yr . However, we note that Earth will receive ^{60}Fe even when the heliosphere is not completely compressed (such as the case today; Koll et al. 2019; Wallner et al. 2020). ^{60}Fe -bearing dust is not deflected by the heliosphere like the ISM gas (smaller-scale dust, $\lesssim 1 \mu\text{m}$, is mediated and shielded by the heliosphere, as shown by Ulysses and Cassini measurements; Sterken et al. 2022). As a result, we expect that the ^{60}Fe timescale is longer than the cloud crossing time. The more quantitative calculations of interstellar ^{60}Fe abundance in atomic form versus dust, dust trajectories in the heliosphere, and heliosphere's response to a changing cloud density profile are outside the scope of this paper.

One interesting aspect is to consider the effect of radiation pressure on dust. Dust coupling to gas, via collisions, is weak. A grain will only be slowed to the gas speed after colliding with about its own mass in gas. For example, for a gas density of 900 cm^{-3} and a grain size of $0.25 \mu\text{m}$ the coupling distance is $\sim 3000 \text{ au}$.

The tighter coupling is via the magnetic field, but then the relevant scale is the gyro radius, which varies strongly with grain size (because the charge-to-mass ratio varies strongly with grain size). For grains larger than about $0.1 \mu\text{m}$ the gyro radius ranges from $\sim 1 \text{ au}$ to $> 10^5 \text{ au}$. For larger grains the gyro radius is larger.

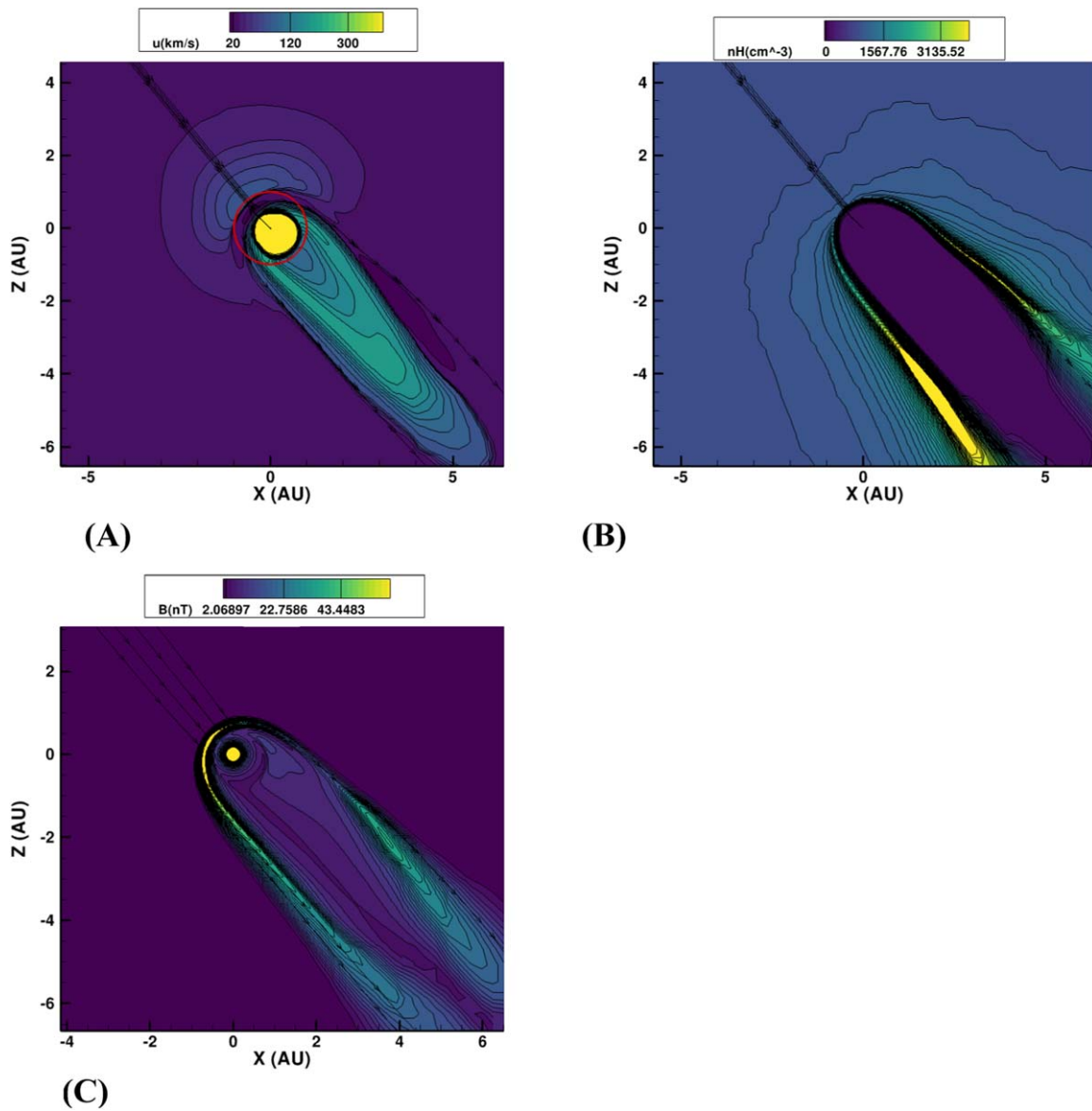


Figure 6. Heliosphere 7 MYA. Panel are shown at the end of simulation at 2.7 yr in the meridional plane at $y = 0$ au (for the model coordinate system see Section 3). Contours are (A) speed (B) neutral hydrogen, and (C) magnetic field. The heliosphere shrinks to 0.7 au at the nose, maintaining a long cometary shape and exposing all planets to cold dense ISM material.

The radiation pressure on the grains is not very significant for grain dynamics. The beta factor, which is the ratio of radiation pressure force to gravitational force on a grain, is mostly < 1 except possibly for grains around $0.2 \mu\text{m}$. So for most grains gravitational attraction is stronger than the radiation force. (see Sterken et al. 2022, and references therein). In general the Lorentz force is much stronger than either the radiation or gravitational forces.

Current models based on benthic paleo records incorporate a complexity of factors. They suggest that ongoing cooling influenced ecosystem structure in the late Miocene (i.e., around 7 MYA) and that a global forcing mechanism must be invoked to explain late Miocene changes (Herbert et al. 2016; Holbourn et al. 2018). Dramatic anomalies in the benthic $\delta^{13}\text{C}$ signals from foraminifera are especially prominent at this time (Westerhold et al. 2020). This again indicates an additional perturbation, or forcing mechanism, contributed to the reported changes in primary production and carbon sequestration—and

may have influenced the potential climate feedback loops involving deep ocean circulation, heat transfer, and alterations in the cryosphere. We propose that ISM exposure due to passage of the solar system through the Local Bubble provides such a forcing mechanism, and that the amplitude and drivers of water temperature changes, and potentially ice volume and extent should be contextualized within time estimates for ISM exposure. Moreover, how ISM exposure might amplify or diminish carbon-cycle circulation and cryosphere feedback should be examined.

In the scenario we have described Earth would have been bathed in excess hydrogen during the ISM contact and in GCRs as the heliosphere shrank upon encountering the Local Bubble's edge. Hydrogen in the upper atmosphere would cause cooling in the mesosphere; it is postulated the midatmosphere (50–100 km) would have been depleted in ozone and as such H eventually cooled the Earth (McKay & Thomas 1978); while in the lower atmosphere H would lead to changes in

greenhouse gas accumulation. Unfortunately, few studies have quantitatively investigated these processes in the context of encounters with dense giant molecular clouds (McKay & Thomas 1978; Yeghikyan & Fahr 2004). Shielding of radiation from outside of our solar system is also clearly of critical importance to climate habitability. Further impacts include mass extinctions (that can be caused by proximity to a supernova; Fields et al. 2020) or potentially deleterious impacts of DNA mutation caused by GCR exposure, which has been the focus for human space travel (Cucinotta & Durante 2006).

Our findings, in combination with new understanding of events circa 2 MYA (Opher et al. 2024), indicate that the location of the Sun in the ISM and more broadly the Local Bubble and regions of cold cloud genesis likely had direct impacts on conditions on Earth with at least two recent periods consistent with ^{60}Fe data. In principle, GCR changes alone could have effects on climate, organismal mutation rates, aging, and extinction rates, and thus broad patterns of diversification. Understanding the extent to which Earth's history is entwined with the travels of the solar system through its neighborhood, including the encounter of Earth with a cold cloud 2 MYA (Opher et al. 2024) and exposure to a dense cold ISM 7 MYA, will shed light on major geologic and biological events, and potentially on long-term trajectories of life on Earth.

Acknowledgments

This work was conceived when M.O. was supported as well by the Fellowship Program, Radcliffe Institute for Advanced Study at Harvard University. This work is supported by NASA grant 18-DRIVE18_2-0029 as part of the NASA/DRIVE program titled “Our Heliospheric Shield,” 80NSSC22M0164. For more information about this center please visit <https://shielddrivecenter.com>.

Appendix

Density of ^{60}Fe on Earth in the Last 10 Million Years

We calculate the surface density of ^{60}Fe collected in the last 10 Myr. We consider that in the scenario of the encounter of heliosphere with the edge of the Local Bubble it encountered a dense cloud similar to the one described Opher et al. (2024). We then proceed by calculating the surface density of ^{60}Fe in a cloud. We assume that (a) all ^{60}Fe is uniformly deposited throughout the cloud so no dust particle pierces through it nor preferentially stopped at surface; (b) the cloud is spherical; and (c) Earth absorbs all ^{60}Fe on its surface when going through cloud.

The density of ^{60}Fe in cloud is:

$$\rho_{60,c} = \frac{M_{60,c}}{V_c} = \frac{M_{60} \left(\frac{R_c^2}{4d_{\text{SN}}^2} \right)}{\left(\frac{4}{3} \right) \pi R_c^3} = \frac{3}{16\pi} \frac{M_{60}}{R_c d_{\text{SN}}^2}, \quad (\text{A1})$$

where M_{60} is the amount (mass) of ^{60}Fe ejected in the supernova, d_{SN} is the distance between the supernova and the cloud, R_c is the radius of the cloud, and V_c the volume of the cloud. We use an ejected ^{60}Fe mass of $3 \times 10^{-5} M_{\odot}$, in agreement with simulations from Sukhbold et al. (2016). The ^{60}Fe half-life is 2.62 Myr.

When Earth encounters the cloud, it travels through a distance l in the cloud, where l ranges from 0 to $2 R_c$. For

simplicity, we parameterize this by writing $l = \beta R_c$ where β can range from 0 to 2 depending on the crossing distance of Earth's trajectory through the cloud (zero when traveling on the tangent line, and two when passing through the middle).

The surface density of ^{60}Fe on Earth is:

$$\begin{aligned} N_{60} &= \frac{M_{60,E}}{4\pi R_E^2} \frac{1}{60u} = \frac{\rho_{60,c} \pi R_E^2 l}{4\pi R_E^2} \frac{1}{60u} = \frac{\rho_{60,c} l}{4} \frac{1}{60u} \\ &= \frac{3\beta}{64\pi} \frac{M_{60}}{d_{\text{SN}}^2} \frac{1}{60u}, \end{aligned} \quad (\text{A2})$$

where we have included the $\frac{1}{60u}$ term to convert from mass density to number density of ^{60}Fe , with u as the atomic mass unit. Finally, we include radioactive decay, where τ is the average lifetime of ^{60}Fe and t is the amount of time after the supernova has exploded, so that the total surface density of ^{60}Fe from a single supernova is:

$$N_{60} = \frac{3\beta}{64\pi} \frac{M_{60}}{d_{\text{SN}}^2} \frac{1}{60u} e^{-\frac{t}{\tau}}. \quad (\text{A3})$$

For multiple supernovae, this expression amounts to the simple sum:

$$N_{60} = \frac{3\beta}{64\pi} \frac{1}{60u} \sum_i \frac{M_{60,i}}{d_{\text{SN},i}^2} e^{-\frac{t}{\tau}}. \quad (\text{A4})$$

This equation does not depend on R_E . This is because a larger planet has a larger cross section to absorb ^{60}Fe ($\sim R_E^2$), but must also spread it out over a larger surface ($\sim R_E^2$). This equation also does not depend on R_c for a similar reason: a larger cloud absorbs more ^{60}Fe ($\sim R_c^2$), but has a lower density ($\sim R_c^{-3}$, distributed through volume, not across surface). Earth must then travel through the cloud ($\sim R_c$). This equation is nearly the same as for a direct transfer (i.e., ^{60}Fe goes straight to Earth), but where the distance is from the supernova to Earth rather than from the supernova to the cloud (Fields & Ellis 1999, Equation (6)). The difference is merely in the preceding constants and the path length through the cloud. Another similar calculation for kilonova enrichment of the proto-Local Bubble has been performed in Wang (2021).

From Zucker et al. (2022) the Local Bubble originated with 15_{-7}^{+11} supernovae. If we assume that all 15 supernovae happened 14 MYA at a distance of 100 pc, the total N_{60} is 3.5×10^7 at cm^{-2} . For a more realistic model, according to Zucker et al. (2022), we model eight supernovae from 14 to 7 MYA, spaced 1 Myr apart. The distances and ^{60}Fe yield are kept the same for all supernovae. We obtain from Equation (A4) the total surface density of ^{60}Fe on Earth, which is $N_{60} = 5.6 \times 10^7$ at cm^{-2} . Figure 7 shows the amount of ^{60}Fe each supernova contributes to the total surface density on Earth. Because the distances and yields are all the same, this plot demonstrates the rate of radioactive decay. The local interstellar fluence (LIF) that the Earth passes through is a factor of 4 larger (the ratio of Earth's cross section to its surface area) such that $N_{60,\text{LIF}} = 2.2 \times 10^8$ at cm^{-2} . Wallner et al. (2021) measured the LIF of the 7 Myr signal as $1.2 \pm 0.4 \times 10^8$ at cm^{-2} . Our value here is slightly higher (factor of ~ 1.9), showing that we can easily recreate the ^{60}Fe surface density as a series of supernovae starting 14 MYA.

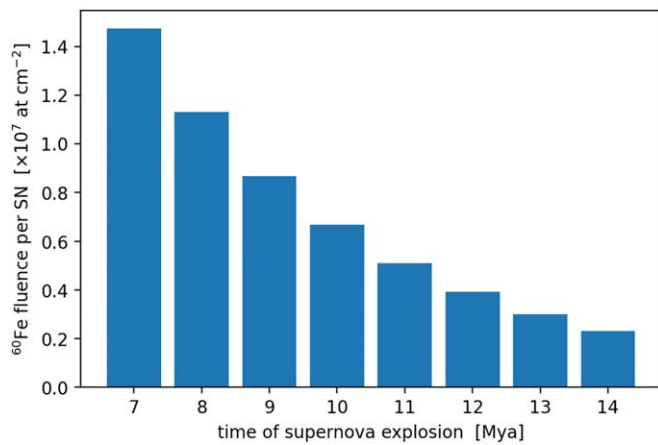


Figure 7. Plot shows the ^{60}Fe fluence contribution of each supernova to the Local Bubble wall prior to the solar system passage.

ORCID iDs

Merav Opher <https://orcid.org/0000-0002-8767-8273>
 Abraham Loeb <https://orcid.org/0000-0003-4330-287X>
 Catherine Zucker <https://orcid.org/0000-0002-2250-730X>
 Alyssa Goodman <https://orcid.org/0000-0003-1312-0477>
 Ralf Konietzka <https://orcid.org/0000-0001-8235-2939>
 Alexandra Z. Worden <https://orcid.org/0000-0002-9888-9324>
 Evan P. Economo <https://orcid.org/0000-0001-7402-0432>
 Jesse A. Miller <https://orcid.org/0000-0001-5071-0412>
 Marc Kornbleuth <https://orcid.org/0000-0002-3479-1766>
 J. E. G. Peek <https://orcid.org/0000-0003-4797-7030>
 Michael M. Foley <https://orcid.org/0000-0002-6747-2745>

References

- Alves, J., Zucker, C., Goodman, A. A., et al. 2020, *Natur*, 578, 237
 Athanassiadou, T., & Fields, B. D. 2011, *NewA*, 16, 229
 Bahcall, J. N., & Bahcall, S. 1985, *Natur*, 316, 706
 Baranov, V. B., Lebedev, M. G., & Ruderman, M. S. 1979, *Ap&SS*, 66, 441
 Begelman, M. C., & Rees, M. J. 1976, *Natur*, 261, 298
 Benincasa, S. M., Loebman, S. R., Wetzell, A., et al. 2020, *MNRAS*, 497, 3993
 Binns, W. R., Israel, M. H., Cummings, A. C., et al. 2016, *Sci*, 352, 677
 Burlaga, L. F. 1984, *SSRv*, 39, 255
 Breitschwerdt, D., Feige, J., Schulreich, M. M., et al. 2016, *Natur*, 532, 73
 Bovy, J. 2015, *ApJSS*, 216, 29
 Cahlon, S., Zucker, C., Goodman, A., et al. 2024, *ApJ*, 961, 153
 Cahlon, S., Zucker, C., Goodman, A., Lada, C., & Alves, J. 2024, *ApJ*, 961, 153
 Clark, P. C., Glover, S. C. O., Ragan, S. E., & Duarte-Cabral, A. 2019, *MNRAS*, 486, 4622
 Cucinotta, F. A., & Durante, M. 2006, *Oncology*, 7, 431
 Dame, T. M., Hartmann, D., & Thaddeus, P. 2001, *ApJ*, 547, 792
 El-Badry, K., Ostriker, E. C., Kim, C.-G., Quaraert, E., & Weisz, D. R. 2019, *MNRAS*, 490, 1961
 Evans, R., Opher, M., Oran, R., et al. 2012, *ApJ*, 756, 155
 Fields, B. D., & Ellis, J. 1999, *NewA*, 4, 419
 Fields, B. D., Athanassiadou, T., & Johnson, S. R. 2008, *ApJ*, 678, 549
 Fields, B. D., Melott, A. L., Ellis, J., et al. 2020, *PNAS*, 117, 21008
 Fimiani, L., Cook, D. L., Faestermann, T., et al. 2016, *PhRvL*, 116, 151104
 Fitoussi, C., Raisbeck, G. M., Knie, K., et al. 2008, *PhRvL*, 101, 121101
 Florinski, V., & Zank, G. 2006, *GeoRL*, 33, L15110
 Foley, M. M., Mocz, P., Burkhart, B., et al. 2024, *ApJ*, submitted
 Fuchs, B., Breitschwerdt, D., de Avillez, M. A., Dettbarn, C., & Flynn, C. 2006, *MNRAS*, 373, 993
 Francis, C., & Anderson, E. 2009, *NewA*, 14, 615
 Frisch, P. C., Bzowski, M., Grun, E., et al. 2009, *SSRv*, 146, 235
 Fry, B. J., Fields, B. D., & Ellis, J. R. 2020, *ApJ*, 894, 109
 Gehrels, N., Laird, C. M., & Jackman, C. H. 2003, *ApJ*, 585, 1169
 Haud, U. 2010, *A&A*, 514, A27
 Herbert, T. D., Lawrence, K. T., Tzanova, A., et al. 2016, *NatGe*, 9, 843
 Holbourn, A. E., Kuhnt, W., Clemens, S. C., et al. 2018, *NatCo*, 9, 1584
 Izmodenov, V. V., & Alexashov, D. B. 2015, *ApJS*, 220, 1432
 Kamdar, H., Conroy, C., Ting, Y.-S., & El-Badry, K. 2021, *ApJ*, 922, 49
 Kerr, F. J., & Lynden-Bell, D. 1986, *MNRAS*, 221, 1023
 Knie, K., Korschinek, G., Faestermann, T., et al. 1999, *PhRvL*, 83, 18
 Knie, K., Korschinek, G., Faestermann, T., et al. 2004, *PhRvL*, 93, 171103
 Koll, D., Korschinek, G., Faestermann, T., et al. 2019, *PhRvL*, 123, 072701
 Konietzka, R., Goodman, A. A., Zucker, C., et al. 2024, *Natur*, 628, 62
 Lallement, R., Babusiaux, C., Vergely, J. L., et al. 2019, *A&A*, 625, A135
 Leike, R. H., Glatzle, M., & Enblin, T. A. 2020, *A&A*, 639, A138
 Linde, T. J. 1998, PhD thesis, Univ. of Michigan
 Loeb, A., & Rybicki, G. B. 1999, *ApJ*, 524, 527
 Ludwig, P., Bishop, S., Egli, R., et al. 2016, *PNAS*, 113, 9232
 McKay, C. P., & Thomas, G. E. 1978, *GeoRL*, 5, 215
 Meyer, D. M., Lauroesch, J. T., Peek, J. E. G., & Heiles, C. 2012, *ApJ*, 752, 119
 Michael, A. T., Opher, M., Toth, G., Tenishev, V., & Borovikov, D. 2022, *ApJ*, 924, 105
 Miller, J. A., & Fields, B. D. 2022, *ApJ*, 934, 32
 Muller, H. R., Frisch, P. C., Florinski, V., & Zank, G. P. 2006, *ApJ*, 647, 1491
 Opher, M., Alouani Bibi, F., Toth, G., et al. 2009, *Natur*, 462, 1036
 Opher, M., Drake, J. F., Swisdak, M., et al. 2011, *ApJ*, 734, 71
 Opher, M., Drake, J. F., Zieger, B., & Gombosi, T. I. 2015, *ApJL*, 800, L28
 Opher, M., Loeb, A., Drake, J., & Toth, G. 2020, *NatAs*, 4, 675
 Opher, M., Richardson, J., Zank, G., et al. 2023, *FrASS*, 10, 1179344
 Opher, M., Peek, J., & Loeb, A. 2024, *NatAs*, 8, 983
 Parker, E. N. 1958, *ApJ*, 128, 664
 Pavlov, A. A., Toon, O. B., Pavlov, A. K., Bally, J., & Pollard, D. 2005, *GRL*, 32, L03705
 Pelgrims, V., Ferriere, K., Boulanger, F., Lallement, R., & Montier, L. 2020, *A&A*, 636, A17
 Schulreich, M. M. 2015, Phd thesis, Berlin Institute of Technology
 Schulreich, M. M., Breitschwerdt, D., Feige, J., & Dettbarn, C. 2017, *A&A*, 604, A81
 Schulreich, M. M., Feige, J., & Breitschwerdt, D. 2023, *A&A*, 680, A39
 Slavin, J. D., Frisch, P. C., Muller, H.-R., et al. 2012, *ApJ*, 760, 46
 Sokolov, I. V., Powell, K. G., Gombosi, T. I., & Roussev, I. I. 2006, *JCoPh*, 220, 1
 Schwadron, N., Moebius, E., Kucharek, H., et al. 2013, *ApJ*, 775, 86
 Springle, V. 2010, *MNRAS*, 401, 791
 Sterken, V. J., Altobelli, N., Kempf, S., et al. 2013, *A&A*, 552, A130
 Sterken, V. J., Baalman, L. R., Draine, B. T., et al. 2022, *SSRv*, 218, 71
 Stone, E. C., Cummings, A. C., McDonald, F. B., et al. 2008, *Natur*, 454, 71
 Stone, E. C., Cummings, A. C., Heikkila, B. C., & Lal, N. 2019, *NatAs*, 3, 1013
 Sukhbold, T., Ertl, T., Woosley, S. E., Brown, J. M., & Janka, H.-T. 2016, *ApJ*, 821, 38
 Toth, G., van der Holst, B., Sokolov, I. V., et al. 2012, *JComS*, 231, 870
 Tchernyshyov, K., & Peek, J. E. G. 2017, *AJ*, 153, 8
 Yeghikyan, A., & Fahr, H. 2004, *A&A*, 425, 1113
 Yeghikyan, A., & Fahr, H. 2006, in Chapter 11 of Solar Journey, the Significance of Our Galactic Environment for the Heliosphere and Earth, ed. P. C. Frisch (Berlin: Springer)
 Wallner, A., Feige, J., Fifield, L. K., et al. 2020, *PNAS*, 117, 21873
 Wallner, A., Feige, J., Kinoshita, N., et al. 2016, *Natur*, 532, 69
 Wallner, A., Froehlich, M. B., Hotchkis, M. A. C., et al. 2021, *Sci*, 372, 742
 Wang, F., Zhang, H.-W., Huang, Y., et al. 2020, *MNRAS*, 504, 199
 Wang, X., Clark, A. M., Ellis, J., et al. 2021, *ApJ*, 923, 219
 Westerhold, T., Marwan, N., Drury, A. J., et al. 2020, *Sci*, 369, 1383
 Zachos, J., Pagani, M., Sloan, L., & Billups, K. 2001, *Sci*, 292, 686
 Zank, G. P., & Frisch, P. C. 1999, *ApJ*, 518, 965
 Zank, G. P. 1999, *SSRv*, 89, 413
 Zucker, C., Alves, J., Goodman, A., Meingast, S., & Galli, P. 2023, in ASP Conf. Ser. 534, Protostars and Planets VII (San Francisco, CA: ASP), 43
 Zucker, C., Goodman, A., Alves, J., et al. 2021, *ApJ*, 919, 35
 Zucker, C., Goodman, A. A., Alves, J., et al. 2022, *Natur*, 601, 334